ACS central science

http://pubs.acs.org/journal/acscii

Research Article

Live-Cell Imaging and Quantification of PolyQ Aggregates by Stimulated Raman Scattering of Selective Deuterium Labeling

Kun Miao and Lu Wei*

Cite This: ACS Cent. Sci. 2020, 6, 478−486

Read Online

ACCESS | Metrics & More | Article Recommendations | Supporting Information

ABSTRACT: Polyglutamine (polyQ) diseases are a group of neurodegenerative disorders, involving the deposition of aggregation-prone proteins with long polyQ expansions. However, the cytotoxic roles of these aggregates remain highly controversial, largely due to a lack of proper tools for quantitative and nonperturbative interrogations. Common methods including *in vitro* biochemical, spectroscopic assays, and live-cell fluorescence imaging all suffer from certain limitations. Here, we propose coupling stimulated Raman scattering microscopy with deuterium-labeled glutamine for live-cell imaging, quantification, and spectral analysis of native polyQ aggregates with subcellular resolution. First, through the enrichment of deuterated glutamine in the polyQ sequence of mutant Huntingtin (mHtt) exon1 proteins for Huntington's disease, we achieved sensitive and specific stimulated Raman scattering (SRS) imaging of carbon−deuterium bonds (C−D) from aggregates without GFP labeling, which is commonly employed in fluorescence microscopy. We revealed that these aggregates became 1.8-fold denser compared to those with GFP. Second, we performed ratiometric quantifications, which indicate a surprising dependence of protein compositions on aggregation sizes. Our further calculations, for the first time, reported the absolute concentrations for sequestered mHtt and non-mHtt proteins within the same aggregates. Third, we adopted hyperspectral SRS for Raman spectroscopic studies of aggregate structures. By inducing a cellular heat shock response, a potential therapeutic approach for inhibiting aggregate formation, we found a possible aggregate intermediate state with changed solvation microenvironments. Our method may hence readily unveil new features and mechanistic insight of polyQ aggregates and pave the way for comprehensive *in vivo* investigations.

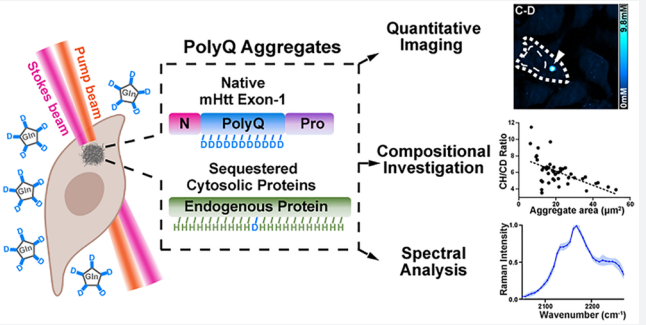

INTRODUCTION

A hallmark of neurodegenerative disorders is the presence of protein aggregates in peripheral nerves.[1−4] Among these disorders are polyglutamine (polyQ) diseases, such as Huntington's disease (HD), which starts with motor symptoms like chorea and is followed by memory deficit and depression.[3,4] The onset of HD has been linked to abnormally expanded CAG trinucleotide repeats that encode the polyQ sequence in mutant Huntingtin (mHtt) proteins. While Q repeats are typically fewer than 37 in healthy humans, they can range from 40 to 250 in Huntington's patients and are consistently found in the protein depositions of HD brain slices by immunohistology.[1,3] However, the pathological roles of polyQ aggregates still remain elusive.[2,4−6] Recent studies suggest that soluble oligomers are cytotoxic by dynamically interacting with cytosolic proteins and triggering apoptosis while aggregates are cytoprotective by sequestering toxic protein oligomers to form stable inclusion bodies.[4,7,8] In contrast, evidence also indicates that toxicity of aggregates arises from depleting functional (e.g., chaperones and transcription factors) and structural (e.g., actin) proteins and impairing cellular organelles (e.g., ribosomes and endoplasmic reticulum).[9−13]

To understand their molecular roles, extensive efforts have been made to investigate the compositions, structures, and kinetics of mHtt aggregates. Conventional biochemical assays and recent quantitative proteomics offer relative protein compositions of the aggregates in reference to the soluble protein pools. However, these methods rely on extensive postprocessing such as aggregation purification and solubilization.[9,10] *In vitro* spectroscopic studies including IR,[14] UV-resonance Raman,[15,16] NMR spectroscopy,[17] and fluorescence[18,19] on model peptides provide crucial information, but they are limited to relatively short expansion lengths because of the difficulty in isolating peptides with long Q repeats.[14−19] More importantly, all these *in vitro* studies cannot recapitulate the native aggregation status in live cells. For live-cell studies, fluorescence imaging offers unprecedented spatial and

Received: November 19, 2019
Published: March 6, 2020

https://dx.doi.org/10.1021/acscentsci.9b01196
ACS Cent. Sci. 2020, 6, 478−486

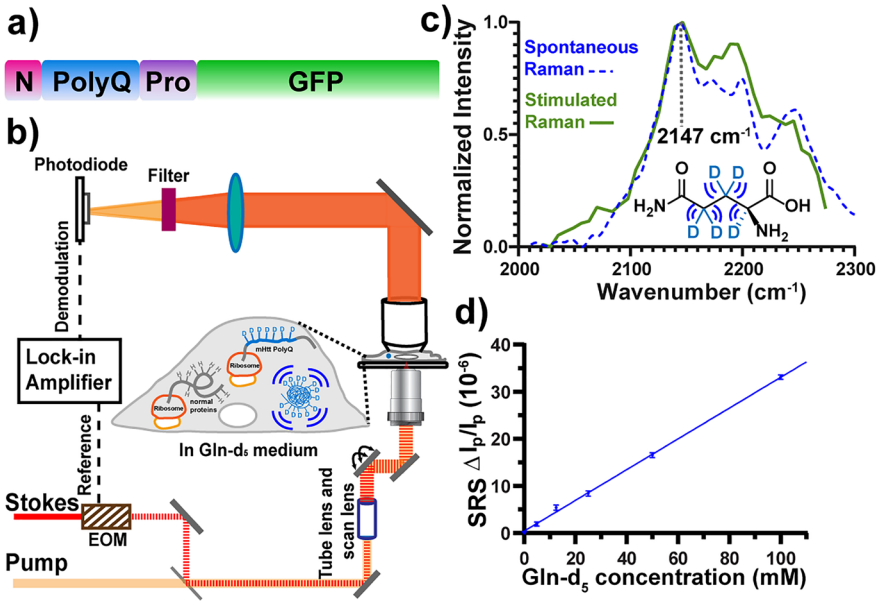

Figure 1. Experimental scheme for stimulated Raman scattering (SRS) microscopy with deuterated glutamine (Gln or Q) labeling. (a) Plasmid construct of a model mutant Huntingtin (mHtt) Exon1 (ex1) protein fused with GFP at the C terminus. N: N-terminal 17 aa fragment. PolyQ: poly glutamine region. Pro: proline-rich domain. GFP: green fluorescent protein. (b) Experimental scheme for SRS imaging of Gln-d_5-labeled polyQ aggregates. (c) Spontaneous Raman (blue dashed) and SRS (green) spectra of 60 mM Gln-d_5 solution. (d) Linear dependence of SRS signals (at 2147 cm^{-1}) on Gln-d_5 concentrations under a 50 μs time constant. Error bar: SD.

temporal resolution, by fusing fluorescent proteins[20] or self-labeling tags (e.g., HaloTag)[21] to the C-terminus of a mHtt exon1 (ex1) sequence (Figure 1a). The aggregation-prone ex1 fragment, which comprises a 17 N-terminal sequence, a polyQ tract followed by a proline-rich domain at the C-terminus (Figure 1a), can effectively induce the pathological phenotype of HD in the transgenic mouse model and humans.[4,22] Compared to mHtt ex1, however, green fluorescent protein (GFP) is much larger in size and has a known tendency to oligomerize.[23] This could perturb the aggregation kinetics and conformations and may contribute to the controversy of reported toxicity. Moreover, because the dense aggregation environment often causes fluorescence quenching,[24] fluorescence imaging is not ideal for quantitative analysis of aggregates. It is therefore highly desirable to have a new modality that combines the advantages from *in vitro* investigations and fluorescence imaging while overcoming their limitations.

Here, we report a novel and general platform for live-cell imaging, quantification, and spectral analysis of polyQ aggregates by stimulated Raman scattering (SRS) microscopy (Figure S1) of deuterium-labeled glutamine (Gln-d_5) (Figure 1b,c). We first achieved specific and sensitive SRS imaging of native polyQ aggregates without the need of large fusion-proteins. We then developed a ratiometric strategy for quantitative analysis of protein content in aggregates of varying sizes. Compared to existing methods, our modality, for the first time, reports the absolute concentrations of both mHtt and non-mHtt proteins from aggregates in live cells. Applying the hyperspectral SRS (hSRS), we further probed the aggregate structures and aggregate−environment interactions upon an induced heat shock response.

RESULTS

Coupling of SRS Microscopy with Deuterated Glutamine Is Ideal for Imaging PolyQ Aggregates.

Labeling of aggregates is achieved through replacing regular Gln in the medium with Gln-d_5 (Figure 1b,c), which would be metabolically incorporated and enriched into the long polyQ tail of expressed mHtt proteins (Figure 1a,b). Targeting the vibrational frequency of carbon−deuterium bonds (C−D), SRS imaging obtains subcellular mapping of mHtt aggregates in live cells. Our strategy has the following advantages: First, the vibrational frequency of C−D in Gln-d_5 (Figure 1c) is in the desired cell-silent region (1800−2600 cm^{-1}), providing high imaging specificity without background from endogenous biomolecules. Second, the nonexchangeable labeling on the C−H side chains of Gln offers reliable signals. Third, Gln enrichment in the polyQ region (Figures 1a) yields both high labeling specificity and superb SRS imaging sensitivity. For example, for a widely used mHtt-97Q ex1 protein, Gln accounts for 68% of the ex1 sequence (Figure S2), while the natural occurrence of Gln is only 4.2% in human proteomes.[25] Compared to label-free SRS[26] and SRS imaging with ^{13}C-phenyalanine[27] or deuterated all essential amino acids,[28] selective Gln-d_5 labeling is significantly more specific for imaging polyQ aggregates. Fourth, compared to using alkyne-tagged unnatural amino acids, which only introduces one tag to one copy of a protein,[29] multiple Q labeling (e.g., 103Q for mHtt-97Q ex1) has higher sensitivity and requires less sample manipulation. Fifth, imaging-wise, compared to spontaneous Raman,[30] SRS provides higher detection sensitivity and faster image acquisition with the stimulated emission quantum amplification principle (Figure S1). Compared to Coherent anti-Stokes Raman scattering (CARS),[31] another nonlinear Raman microscopy technique, SRS, offers high-fidelity Raman spectra (Figure 1c) and linear concentration dependence (Figure 1d) without a nonresonance background.

We first determined our SRS detection limit on Gln-d_5 solution to be 3 mM (Figure 1d, when signal (S)/noise (N) = 1) by targeting the C−D peak at 2147 cm^{-1}. Hence, our detection limit is as low as 29 μM for mHtt proteins with a

https://dx.doi.org/10.1021/acscentsci.9b01196
ACS Cent. Sci. 2020, 6, 478−486

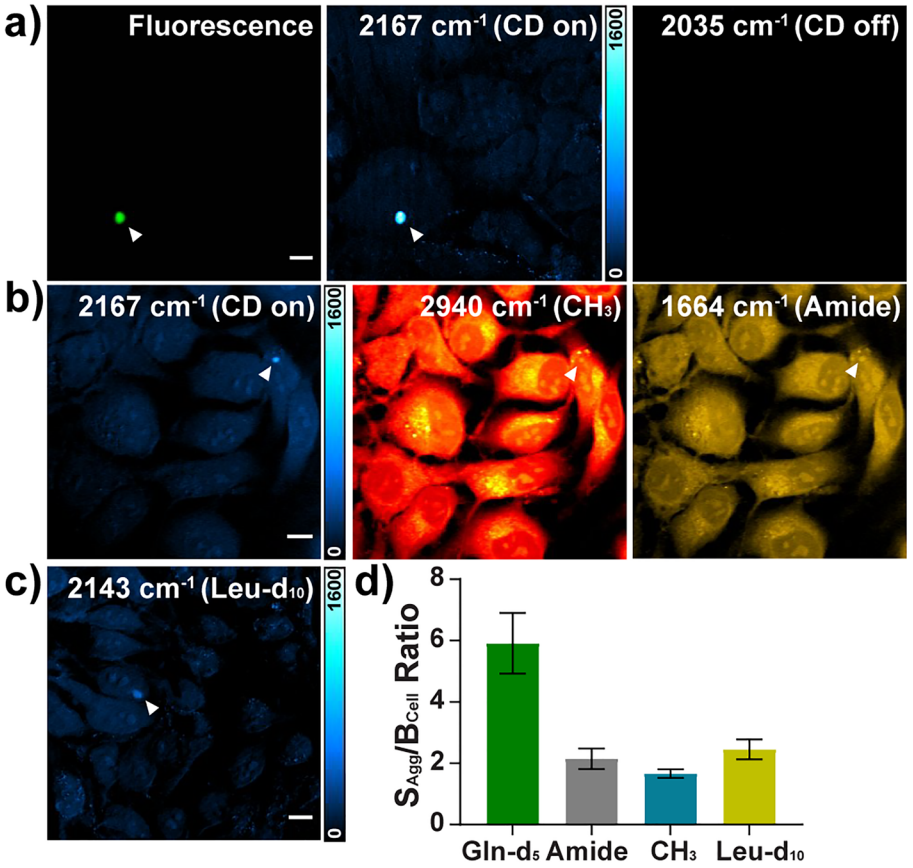

Figure 2. Live-cell SRS imaging of mHtt-97Q-GFP aggregates with Gln-d_5 labeling. (a) SRS imaging of mHtt aggregates (arrowheaded, 2167 cm^{-1}, C−D on), validated by fluorescence imaging through GFP (Fluorescence). Off-resonance image at 2035 cm^{-1} shows no signal. (b) Live-cell SRS images for an mHtt-97Q-GFP aggregate (arrowheaded) at Gln-d_5 (2167 cm^{-1}), CH_3(2940 cm^{-1}), and amide I (1664 cm^{-1}) channels on the same set of HeLa cells. (c) SRS imaging of an mHtt-97Q-GFP aggregate at 2143 cm^{-1} by leucine-d_{10} (Leu-d_{10}) labeling. (d) Average S_{agg}/B_{cell} from SRS images of C−D with Gln-d_5 labeling (5.75 ± 1.03, n = 13); amide I (2.15 ± 0.34, n = 4); CH_3 (1.66 ± 0.14, n = 10); and C−D with Leu-d_{10} labeling (2.45 ± 0.33, n = 10). Error bar: SD.

total of 103 Gln in the mHtt-97Q ex1 protein. This strategy offers higher detection sensitivity compared to previously reported 200 μM by SRS imaging of alkyne tags.[32] In cells, however, the detection limit is set by aggregate-signal to cellular-background ratio (S_{agg}/B_{cell}). There are two sources for B_{cell}. First, the newly synthesized proteome incorporates Gln. Since Gln accounts for 4.2% of human proteome,[25] the estimated detectability for mHtt-97Q ex1 is 86 μM when S_{agg}/B_{cell} = 1 (details in the SI). Second, the intracellular free Gln pool is about 8 mM,[33] slightly lowering the achievable detectability. To minimize this additional background, we replaced the medium with buffer before imaging. Although a detection sensitivity of 86 μM may be too high for imaging normal proteins, it is highly feasible to detect polyQ aggregates down to very small sizes. Our GFP fluorescence analysis by time-lapse tracking of mHtt-97Q-GFP proteins (Figure S3a,b) and tetramethylrhodamine (TMR) fluorescence analysis of mHtt-97Q-Halo proteins (Figure S3c) suggest that once the new and small aggregates form in cells, the concentration of polyQ protein is already beyond 86 μM to as high as 400 μM.

Imaging and Quantification of mHtt Aggregates with and without GFP Labeling in Live HeLa Cells. We next validated our SRS imaging by transfecting HeLa cells with mHtt-97Q-GFP plasmid (Figure 1a and Figure S2) and culturing them in Gln-d_5 medium. We first conducted parallel SRS and fluorescence imaging on the same set of live cells. The SRS image of C−D enriched aggregate (Figure 2a, 2167 cm^{-1}) agrees well with the fluorescence image of GFP (Figure 2a, fluorescence). A clear off-resonance image demonstrates high SRS imaging quality (Figure 2a, 2035 cm^{-1}). The C−D peak for Gln-d_5 is shifted from 2147 cm^{-1} in solution to 2167 cm^{-1} after being incorporated into cellular proteins, suggesting a change of the microenvironment. Indeed, we found that the shifted C−D spectrum has Raman spectral features from both Gln-d_5 solution and solid (peaked at 2167 cm^{-1}) (Figure S4). As a comparison, label-free SRS images at CH_3 (2940 cm^{-1}) and amide I (1664 cm^{-1}) channels, widely adopted for imaging total proteins,[26] show much decreased detection specificity, particularly pronounced for small aggregates (Figure 2b, arrow indicated), which are indistinguishable from the nucleoli. Moreover, the high contrast of the C−D image decreases significantly if Gln-d_5 is replaced by nonenriched leucine-d_{10} (Leu-d_{10}) for labeling (Figure 2c). Our quantification on the average S_{agg}/B_{cell} for each channel clearly demonstrated much higher imaging specificity with Gln-d_5 (Figure 2d).

After establishing the feasibility for SRS imaging of Gln-d_5-labeled mHtt-97Q-GFP aggregates, we aimed to image native mHtt-97Q proteins without GFP (Figure 3a). GFP may perturb aggregation formation of mHtt proteins, because it is 238 amino acid (aa) in length, which is about twice as large as mHtt-97Q ex1 with only 152 aa. We successfully imaged aggregates at the same C−D frequency (Figure 3b, CD on and

https://dx.doi.org/10.1021/acscentsci.9b01196
ACS Cent. Sci. 2020, 6, 478−486

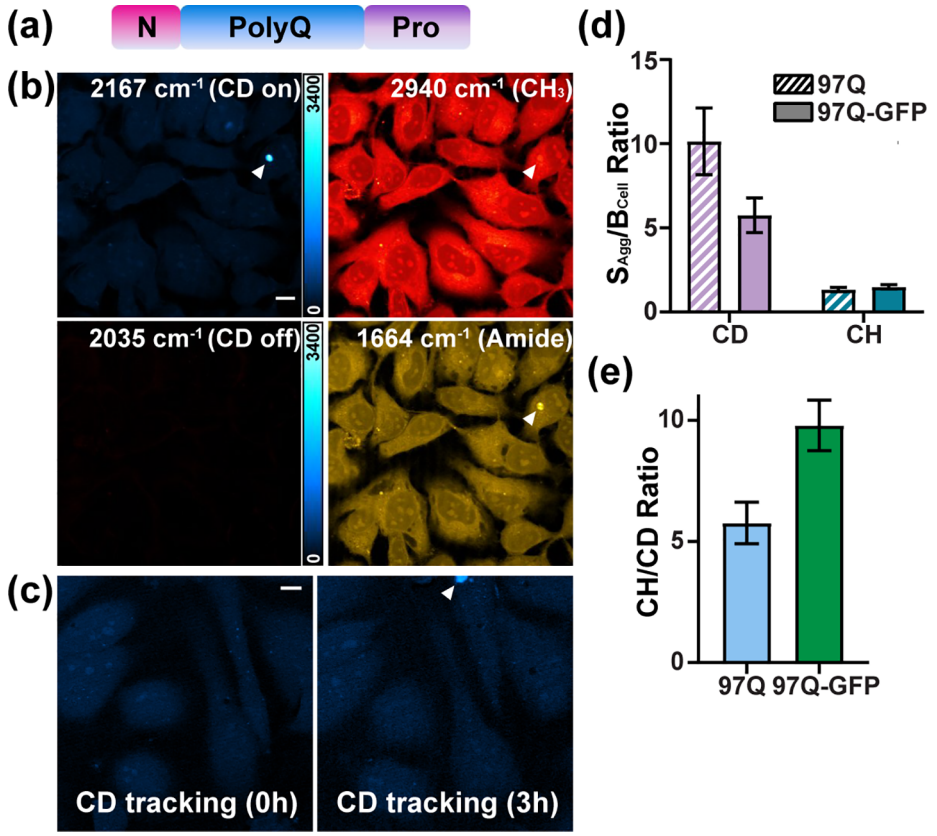

Figure 3. SRS imaging of mHtt-97Q aggregates without GFP. (a) Plasmid construct of mHtt-97Q by deleting GFP sequence. (b) SRS images of a Gln-d_5-labeled aggregate at C−D on-resonance (2167 cm^{-1}), C−D off-resonance (2035 cm^{-1}), CH_3 (2940 cm^{-1}), and amide I (1664 cm^{-1}). (c) Time-lapse SRS tracking at the C−D channel for capturing aggregation formation on the same set of live cells. (d) S_{agg}/B_{cell} of mHtt-97Q (97Q) in C−D (CD, 10.14 ± 1.99, n = 11) and CH_3 (CH, 1.50 ± 0.12, n = 10) channels compared to that for mHtt-97Q-GFP (97Q-GFP, CD, 5.75 ± 1.03, n = 13; CH, 1.66 ± 0.14, n = 10). (e) CH/CDs for 97Q-GFP (9.79 ± 1.05, n = 7) and 97Q (5.75 ± 0.86, n = 20) aggregates. Scale bar: 10 μm. Error bar: SD.

off). Interestingly, these aggregates (Figure 3b, 2167 cm^{-1}) are about twice as bright as those of similar sizes with GFP labeling (Figure 2a, 2167 cm^{-1}). Because the GFP sequence only contains 8 Gln, the C−D intensity should remain approximately unchanged when deleting GFP. We hence reasoned that the detected intensity increase is due to the formation of denser aggregates. A similar phenomenon was recently reported by Cryo-ET with the same mHtt ex1 sequence.[11] To test our theory, we acquired amide I images to compare total protein concentrations between aggregates with and without GFP. If the density remains unchanged, mHtt-97Q aggregates would have a much lower amide intensity than mHtt-97Q-GFP because the GFP sequence contributes significantly to amide signals. We observed similar levels of amide signals between these two types of aggregates (Figure S5), confirming that the increase in aggregate density makes up for the signal loss of deleting GFP. Moreover, mHtt-97Q aggregates become barely distinguishable from cellular background in the CH_3 channel (Figure 3b, 2940 cm^{-1}), indicating that previous CH_3 signals for aggregates were mainly from the GFP sequence (Figure 2b, 2940 cm^{-1}, and Figure S2). To prove the high biocompatibility of our method, we also demonstrated time-lapse SRS imaging on the same set of live cells to capture the aggregation formation (Figure 3c). To quantify aggregates from multiple experimental replicates, we plotted the average S_{agg}/B_{cell} in both C−D and CH channels for mHtt-97Q and mHtt-97Q-GFP aggregates (Figure 3d). In the C−D channel, the S_{agg}/B_{cell} for mHtt-97Q aggregates is 1.8-fold higher, confirming the formation of 1.8-fold denser aggregates without GFP labeling, as B_{cell} is not affected by the change of plasmids. In the C−H channel, the S_{agg}/B_{cell} values remain approximately the same. We further confirmed our high detection specificity of polyQ aggregates by inducing the formation of stress granules in normal HeLa cells and confirmed that our SRS imaging with Gln-d_5 labeling does not detect these non-polyQ-aggregate-type of stress granules (Figure S6). Going beyond mHtt-97Q, we imaged and quantitatively analyzed a shorter Q expansion sequence, mHtt-46Q, for which the Q number is just above the disease-prone aggregation threshold (Figure S7). Similarly, we found that mHtt-46Q aggregates are about 1.6-time denser compared to those formed by mHtt-46Q-GFP. Moreover, we demonstrated our applicability of imaging polyQ aggregates in a stable embryonic stem cell-line[34] (Figure S8), paving the way for more general future applications.

Ratiometric Quantifications for the Dependence of Protein Compositions on Aggregation Sizes. The feature of parallel C−D and CH_3 SRS imaging enables us to perform ratiometric analysis of CH_3-to-CD ratios (CH/CDs) to investigate polyQ aggregate compositions of non-mHtt and mHtt proteins. This is because the CD signals are from Gln-d_5, which mainly originates from mHtt proteins, while the CH_3 signals represent non-Gln aa, which come from the combined sources of non-Gln aa in mHtt proteins and sequestered non-

https://dx.doi.org/10.1021/acscentsci.9b01196
ACS Cent. Sci. 2020, 6, 478−486

mHtt proteins. We first applied CH/CD quantifications on both mHtt-97Q-GFP and mHtt-97Q aggregates (Figure 3e). Surprisingly, the average CH/CD remains as high as 5.75 for mHtt-97Q aggregates (Figure 3e). If the aggregates were formed primarily by mHtt proteins, the CH/CD should be about 0.5 because the mHtt-97Q sequence contains 49 non-Q aa and 103 Q. Similarly, the CH/CD should have decreased by 5-fold from mHtt-97Q-GFP (289 non-Q aa and 112 Q) to mHtt-97Q aggregates (49 non-Q aa and 103 Q) (Figure S2). Instead, the decrease is only 1.5-fold (Figure 3e, 9.79 vs 5.75). Our control experiments confirmed that the Gln-d_5 labeling efficiency is close to 100% (i.e., *de novo* glutamine synthesis for regular Gln is about zero, Figures S9 and S10), indicating that all 103 Q in the mHtt sequence are deuterated. Our results hence imply that these aggregates contain a rather high percentage of non-mHtt proteins. Sequestrations and depletions of cellular functional and structural proteins by aggregates have been suggested to be one underlying mechanism of HD cytotoxicity.[9−13] Consequently, we calculated the relative molar percentages for mHtt and non-mHtt proteins in the aggregates. Assuming that the molar percentage of mHtt and non-mHtt proteins in the aggregates is x and $1 - x$, respectively, with known protein sequences, we can generate an equation with x and $(1 - x)$ for the relative ratio between non-Gln aa and Gln-d_5 to represent the measurable of CH/CDs (Figure 3e) (details in the SI). We calculated that the average molar percentage of non-mHtt proteins is indeed as high as 54% for an average CH/CD of 5.75.

Now that we have established that CH/CDs could serve as a direct indicator of aggregation compositions, we next examined the relationship between CH/CDs and aggregation sizes. Based on the sequestration theory,[12,13] we expect that the relationship might offer insight for understanding the molecular cytotoxicity of polyQ aggregates. Interestingly, we observed a negative correlation (Figure 4a, Pearson's $r = -0.56$), which indicates that the percentage of sequestered mHtt proteins increases as the aggregates grow. As a comparison, such distinctive correlation by Gln-d_5 labeling is absent when replaced by Leu-d_{10} labeling (Figure 4b, Pearson's $r = -0.11$), because mHtt and non-mHtt proteins have similar leucine abundance. This underscores the importance of specific polyQ labeling to observe such a size−composition correlation.

In addition to calculating molar percentages from CH/CDs, we can also compute absolute concentrations with aggregate intensities in the C−D channel and our reference calibration curves (Figure 1d). Such quantification is otherwise highly challenging for existing methods. We selected three representative aggregates with different sizes for calculation (Figure 4a, color-indicated, details in the SI and results listed in Table S1). The mHtt protein concentration in the small aggregate (Figure 4a, green dot) ranges from 1.2 to 2.1 mM (Figure 4c, 6.7 μm^2). It increases to 4.3−5.1 mM (and Figure 4d, 19.1 μm^2) for the medium aggregate (Figure 4a, red dot). The concentration becomes 5.6−6.4 mM for the large aggregate (36.5 μm^2, Figure 4a, magenta dot). The upper and lower limits shown are determined by the relative content of newly synthesized and pre-existing non-mHtt proteins sequestered to the aggregates. Surprisingly, we found that while mHtt concentrations increase with aggregate sizes, the concentrations of non-mHtt proteins remain almost the same for small (4.6 mM), medium (4.7 mM), and large (4.2 mM) aggregates (Table S1). Our observations therefore suggest that the formation of small aggregates preferentially sequesters non-

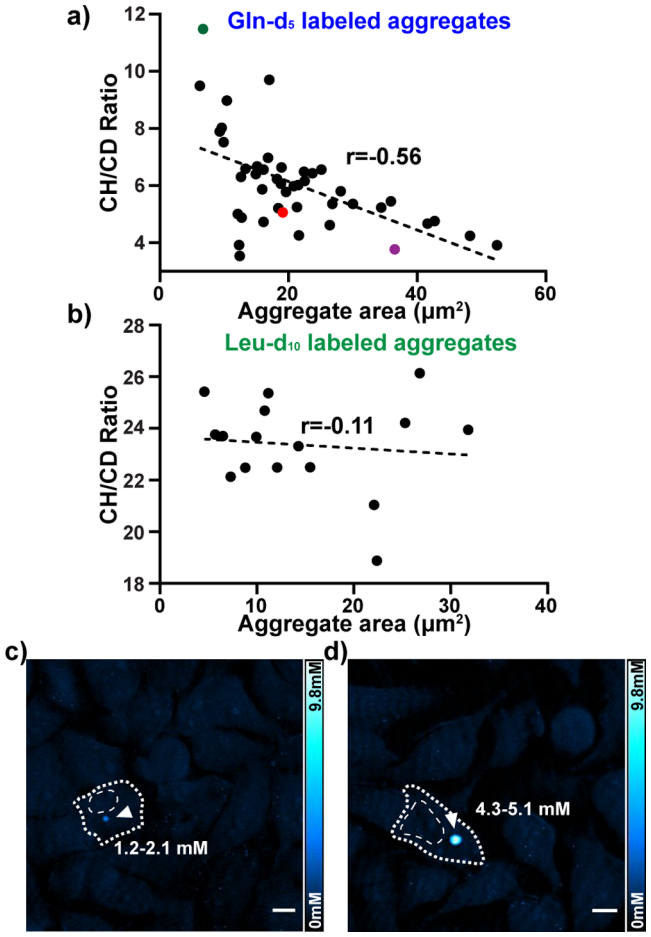

Figure 4. SRS quantification for mHtt-97Q aggregates of different sizes. (a) CH/CDs for Gln-d_5-labeled aggregates present a negative correlation on aggregation areas (Pearson's coefficient $r = -0.56$). (b) Minimum correlation between CH/CDs for Leu-d_{10}-labeled aggregates and aggregation areas (Pearson's coefficient $r = -0.11$). (c, d) C−D SRS images for representative Gln-d_5-labeled small (c, 6.7 μm^2, green dot in a) and medium (d, 19.1 μm^2, red dot in a) mHtt-97Q aggregates. Calculated mHtt-97Q concentrations for the aggregates are indicated. Cell shapes and nuclei are outlined by a white dotted line. Scale bar: 10 μm.

mHtt cytosolic proteins (to as high as 70%). These proteins are likely functional chaperones, ribonucleoproteins, and structural proteins.[9−13] As the aggregates become larger, they then sequester more mHtt proteins. This might indicate a cellular rescue mechanism during aggregate growth by clearing toxic mHtt proteins.[4,7,8] Our data further demonstrate that the total protein concentrations of these aggregates fall in the range 5−10 mM. To the best of our knowledge, our study is the first to quantify the mHtt protein concentrations and molar percentages for aggregates of different sizes in live cells.

Interrogating Aggregate Structures and Aggregate−Environment Interactions by Hyperspectral SRS (hSRS) Imaging. One key advantage for *in vitro* spectroscopic studies over live-cell fluorescence imaging is that they provide structural and conformational information on the aggregates.[14−19] For instance, multiple reports suggested the presence of β-sheet-rich structures in mHtt aggregates. However, there is still no consensus.[15,18] We therefore adopted hSRS to analyze mHtt-97Q aggregates in live cells. We started with the amide I band since its Raman vibration is well

https://dx.doi.org/10.1021/acscentsci.9b01196
ACS Cent. Sci. 2020, 6, 478−486

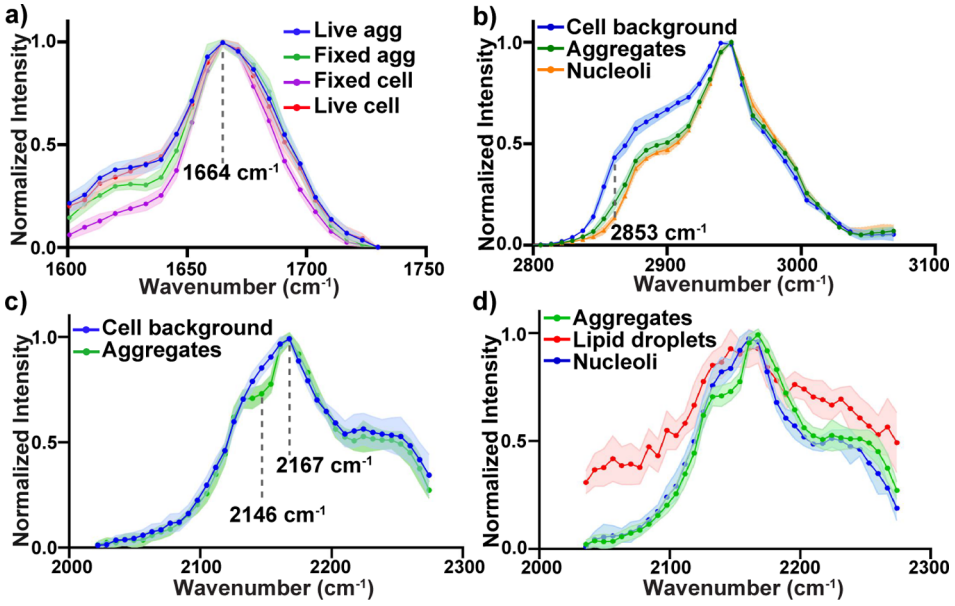

Figure 5. Hyperspectral SRS analysis on mHtt-97Q aggregates. (a) Average amide I SRS spectra of live aggregates (Live agg, blue, n = 14), live cell-background (Live cell, red, n = 14), fixed aggregates (Fixed agg, green, n = 10), and fixed cell-background (Fixed cell, magenta, n = 10). (b) Live-cell SRS CH_3 spectra of aggregates (green, n = 14), cell background (blue, n = 16), and nucleoli (orange, n = 16). (c) Live-cell SRS C−D spectra of Gln-d_5-labeled aggregates (green, n = 20) and cell background (blue, n = 20). (d) Live-cell SRS C−D spectra on small mHtt aggregates (green, n = 20), lipid droplets (red, n = 10), and nucleoli (blue, n = 12) with distinct spectral features. Error bar: SD.

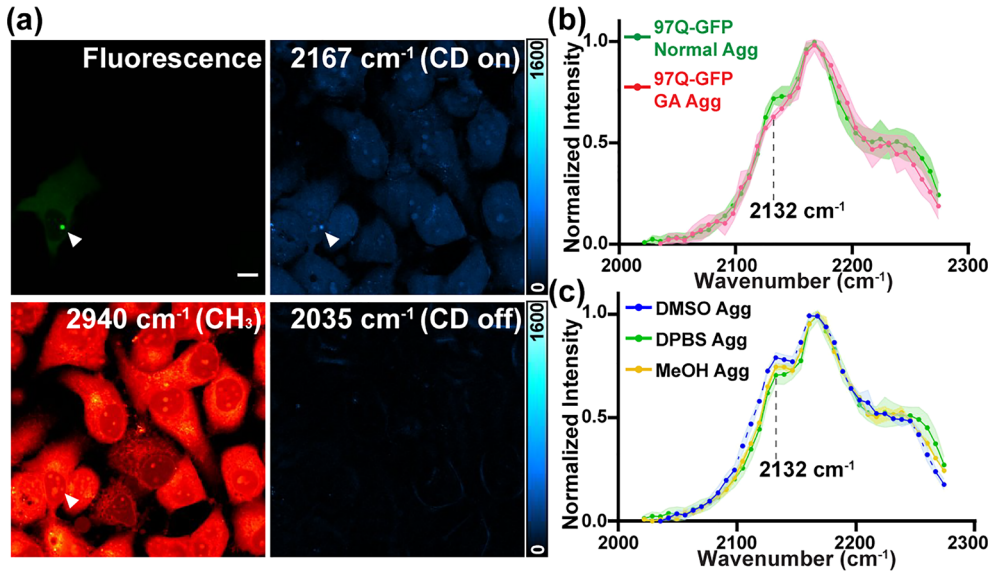

Figure 6. Hyperspectral SRS study of mHtt aggregations upon cellular heat shock responses. (a) Fluorescence (green) and correlative SRS images for mHtt-97Q-GFP aggregates (white arrowheaded) at 2167 cm^{-1} (C−D on-resonance), 2035 cm^{-1} (off-resonance), and 2940 cm^{-1} (CH_3) in live cells after 100 nM geldanamycin (GA) treatment for 20 h. Scale bar: 10 μm. (b) SRS spectra of normal mHtt aggregates (green, n = 20) and a subset of GA-treated small aggregates (red, n = 7). (c) SRS spectra of mHtt aggregates in fixed cells in DPBS buffer (green, n = 15), MeOH (yellow, n = 5), and DMSO (blue, n = 6). Error bar: SD.

documented for probing protein secondary structures by vibrational spectroscopy.[16] A recent report by label-free hSRS imaging of amide I on amyloid plaques in brain tissues revealed a clear 12 cm^{-1} blue shift (resolvable by our spectral resolution of ~12 cm^{-1}), which corresponds to cross-β sheet structures.[35] Nonetheless, we observed no such difference comparing the amide I spectrum of mHtt aggregates to that of the cellular background (Figure 5a, 1664 cm^{-1}, blue vs red). Similar to a recent study,[18] our data suggest that β-sheet structures might not be enriched in these aggregates. Note that we detected a spectral distortion upon chemical fixation (Figure 5a, from 1600 to 1640 cm^{-1}, green vs blue and magenta vs red), highlighting the importance of live-sample analysis.[35,36] Similar to amide I, CH_3 (2940 cm^{-1}) offers no discernible spectral information (Figure 5b), since the signals mainly come as sequestered non-mHtt proteins. The aggregates' spectra are almost identical to those of nucleoli with abundant proteins and rRNA. The lower shoulder at 2850 cm^{-1}, attributed to CH_2 vibrations, implies reduced lipids in the aggregates.

https://dx.doi.org/10.1021/acscentsci.9b01196
ACS Cent. Sci. 2020, 6, 478−486

We next asked whether the C−D spectral region could offer insightful structural information with specific aggregate labeling. Interestingly, we observed a clear dip around 2146 cm^{-1} from aggregates compared to that from the cellular background (Figure 5c), suggesting a structural or microenvironmental difference between aggregated and cytosolic mHtt proteins. To understand such spectral changes, we fitted the averaged spectra (Figure 5c) by three Lorentzian peaks (Figure S11a,b). Our results indicate that the observed 2146 cm^{-1} dip resulted from the narrowing and the slight red shift of the shoulder peak at 2130 cm^{-1} (Figure S11c,d). The narrowing of the peak width is likely due to the formation of a more ordered structure upon aggregation.[16] Our results establish that this shoulder peak could serve as a sensitive indicator for the microenvironment of mHtt aggregates. We note that the weak-intensity cellular background structures, including nucleoli and lipid droplets shown in the C−D images, might interfere with the specific analysis of small aggregates with low signals. In this case, C−D spectra generated by hSRS on aggregates, nucleoli, and lipid droplets could help unequivocally differentiate these structures (Figure 5d).

As we have proven our technique as an effective method to analyze the microenvironment of native aggregates, we sought to apply it to understanding molecular interactions between polyQ aggregates and heat shock proteins (HSPs), key chaperones for protein folding and inhibiting protein aggregations.[37] This may offer fundamental insight toward therapeutic development for HD.[6] We induced cellular heat shock responses by a small-molecule drug, geldanamycin (GA), an inhibitor of HSP 90, which has been shown to effectively induce the expression of HSP 40 and 70 for the clearance of polyQ aggregates.[37] We first validated the function of GA by confirming that the number of large aggregates decreases with the treatment of increased GA concentrations[37] (Figure S12). We next resorted to C−D hSRS on mHtt-97Q aggregates. Interestingly, in GA-treated samples, we discovered a subset of aggregates with reduced size and intensity that consistently present a varied spectral feature with a lowered shoulder peak at 2132 cm^{-1} compared to that of larger-size aggregates (Figure S13a,b). Inspired by this spectroscopic observation, we came back to mHtt-97Q-GFP and adopted a correlative fluorescence and hSRS to understand this phenomenon (Figure 6a). We found that such aggregates, when exhibiting the same SRS spectral feature as found for the mHtt-97Q subset (Figure 6b and Figure S13c), always coexist with surrounding diffusive mHtt protein pools (Figure 6a, Fluorescence). Recently, a liquid-to-solid phase transition is reported for the mHtt-97Q-GFP proteins during aggregation formation.[38] We first speculated that our observed shoulder peak decrease is caused by a reverse phase conversion from solid mHtt aggregates toward the surrounding liquid pool by GA triggered upregulation of HSP 40/70. However, the fluorescence loss in photobleaching (FLIP) experiments on the surrounding fluorescent pool did not reveal any fluorescence exchange between the cytosolic and aggregated mHtt proteins (Figure S14), ruling out our phase-transition hypothesis.

Since C−D vibration is sensitive to the microenvironment, similar to that from CH,[39] we then asked whether such a decrease at the 2132 cm^{-1} shoulder peak corresponds to a change of secondary structures when interacting with HSP 40/70 proteins, as suggested by previous *in vitro* EM experiments.[40] To test the hypothesis, we emerged fixed non-GA-treated cells containing mHtt-97Q-GFP aggregates in solvents with descending hydrogen-bonding capacity (Figure 6c, from DPBS buffer (green), to MeOH (yellow) and DMSO (blue)). Interestingly, the 2132 cm^{-1} shoulder increases accordingly (Figure 6c, vertical line). Quantitative fittings for the averaged spectra with three Lorentzian peaks (Figure S15a−c) further confirmed an increase of ratios between the shoulder (2130 cm^{-1}, peak1) and the major (2169 cm^{-1}, peak2) peaks (Figure S15e,f) from DPBS-treated aggregates (Figure S15a) to DMSO-treated aggregates (Figure S15c). This indicates that the peak1/peak2 ratios may report the local solvation states (e.g., hydrogen bonding) of aggregates. Similar fitting for the averaged spectrum from GA-treated aggregates (Figure S15d) showed that it poses the lowest peak1/peak2 ratio (Figure S15e,f), suggesting that the local solvation environment for our captured GA-treated aggregates may be more hydrogen-bonded compared to that for regular cellular proteomes (Figure S15d). Such likely hyperhydration status might be caused by a partially folded state, a folding intermediate, for aggregates upon interacting with HSP 40/70 in live cells.[41] We further analyzed the CH/CD ratios on these small aggregates in cells with and without induced heat-shock responses. We postulated that if the heat-shock responses recruit extra HSPs to the aggregates, as our hSRS data suggested above, we might detect an increase in CH/CD ratios since the percentage of the non-mHtt proteins is higher in these aggregates. We indeed found that the CH/CD ratios became slightly higher in small aggregates from cells under induced heat-shock responses compared to those in similarly sized aggregates from noninduced cells (Figure S16).

CONCLUSIONS

In summary, we demonstrated the combination of SRS microscopy with Gln-d_5 labeling to be a general platform for sensitive and specific imaging, ratiometric quantification, and hyperspectral analysis of native polyQ aggregates in HD. Our technique provides new and complementary structural and compositional information to our current knowledge of polyQ aggregates. As shown above, our detection sensitivity and specificity are ensured from three aspects. First, the expanded polyQ sequences yield a Gln-d_5 labeling enrichment in disease proteins over the normal proteins with only low Q abundance. Second, the formation of the aggregates is specifically induced by these disease-form polyQ proteins. Together, these ensure a much higher signal from polyQ aggregates compared to that from the cellular background. Third, in the case the aggregates are small with low signals, hSRS on aggregates adds an additional layer of spectral specificity, differentiating the aggregates from other puncta-like structures, including nucleoli and lipid droplets.

Our method is also applicable to polyQ expansions of various lengths. In particular, with linear concentration dependence, it is suited for investigating aggregates of extended polyQ construct (e.g., >200Q), which may form rather dense structures and pose challenges to study by other strategies. Our method is also applicable to other polyQ diseases, including spinocerebellar ataxia and spinobulbar muscular atrophy.[42] Other poly aa diseases[43,44] with poly-glycine-alanine (poly-GA), poly-proline-arginine (poly-PR), and poly-proline-alanine (poly-PA) aggregates, recently reported in the ALS/FTD patient brain, could also be investigated by selective deuteration of corresponding aa. To better guide future SRS work on these aggregates, we further calculated the corresponding SRS detection limits for

https://dx.doi.org/10.1021/acscentsci.9b01196
ACS Cent. Sci. 2020, 6, 478−486

representative, varying lengths of polyQ and poly aa sequences (Table S2). In addition, since Gln can transport across the blood−brain barrier,[45] and deuterium labeling is minimally invasive, applications to animal models or even to humans may be possible. Moreover, correlative live-cell SRS imaging with Gln-d_5 labeling with recently demonstrated Cryo-ET[11] or quantitative proteomics[12] may offer a comprehensive structure−function relationship for native mHtt-97Q aggregates.

■ ASSOCIATED CONTENT

Supporting Information

The Supporting Information is available free of charge at https://pubs.acs.org/doi/10.1021/acscentsci.9b01196.

Detailed experimental procedures, calculations for detection limits and compositional analysis, supplementary tables, and supplementary figures (PDF)

■ AUTHOR INFORMATION

Corresponding Author

Lu Wei − *Division of Chemistry and Chemical Engineering, California Institute of Technology, Pasadena, California 91125, United States;* orcid.org/0000-0001-9170-2283; Email: lwei@caltech.edu

Author

Kun Miao − *Division of Chemistry and Chemical Engineering, California Institute of Technology, Pasadena, California 91125, United States;* orcid.org/0000-0001-6567-3650

Complete contact information is available at: https://pubs.acs.org/10.1021/acscentsci.9b01196

Notes

The authors declare no competing financial interest.

■ ACKNOWLEDGMENTS

We would like to thank Dr. C. Qian, D. Lee, J. Du, and Dr. L. Voong for helpful discussions. We are grateful for the plasmid (mHtt-97Q-GFP) shared by Prof. R. Kopito and Prof. F.-U. Hartl. We thank Prof. Z. Liu for sharing the stable embryonic stem cell-lines. L.W. acknowledges the support of start-up funds from California Institute of Technology.

■ REFERENCES

(1) Paulson, H. Protein fate in neurodegenerative proteinopathies: polyglutamine diseases join the (mis)fold. *Am. J. Hum. Genet.* **1999**, *64*, 339−345.

(2) Hipp, M. S.; Park, S.-H.; Hartl, F. U. Proteostasis impairment in protein-misfolding and -aggregation diseases. *Trends Cell Biol.* **2014**, *24* (9), 506−514.

(3) Bates, G. Huntingtin 1aggregation and toxicity in Huntington's disease. *Lancet* **2003**, *361* (9369), 1642−1644.

(4) Finkbeiner, S. Huntington's disease. *Cold Spring Harbor Perspect. Biol.* **2011**, *3*, No. a007476.

(5) Sahl, S. J.; Lau, L.; Vonk, W. I. M.; Weiss, L. E.; Frydman, J.; Moerner, W. E. Delayed emergence of subdiffraction-sized mutant Huntingtin fibrils following inclusion body formation. *Q. Rev. Biophys.* **2016**, *49* (e2), 1−13.

(6) Eisele, Y. S.; Monteiro, C.; Fearns, C.; Encalada, S. E.; Wiseman, R. L.; Powers, E. T.; Kelly, J. W. Targeting protein aggregation for the treatment of degenerative diseases. *Nat. Rev. Drug Discovery* **2015**, *14* (11), 759−780.

(7) Ramdzan, Y. M.; Trubetskov, M. M.; Ormsby, A. R.; Newcombe, E. A.; Sui, X.; Tobin, M. J.; Bongiovanni, M. N.; Gras, S. L.; Dewson, G.; Miller, J. M. L.; et al. Huntingtin inclusions trigger cellular quiescence, deactivate apoptosis, and lead to delayed necrosis. *Cell Rep.* **2017**, *19* (5), 919−927.

(8) Arrasate, M.; Mitra, S.; Schweitzer, E. S.; Segal, M. R.; Finkbeiner, S. Inclusion Body Formation Reduces Levels of Mutant Huntingtin and the Risk of Neuronal Death. *Nature* **2004**, *431* (7010), 805−810.

(9) Hosp, F.; Gutiérrez-Ángel, S.; Schaefer, M. H.; Cox, J.; Meissner, F.; Hipp, M. S.; Hartl, F.-U.; Klein, R.; Dudanova, I.; Mann, M. Spatiotemporal proteomic profiling of Huntington's disease inclusions reveals widespread loss of protein function. *Cell Rep.* **2017**, *21* (8), 2291−2303.

(10) Suhr, S. T.; Senut, M.-C.; Whitelegge, J. P.; Faull, K. F.; Cuizon, D. B.; Gage, F. H. Identities of sequestered proteins in aggregates from cells with induced polyglutamine expression. *J. Cell Biol.* **2001**, *153* (2), 283−294.

(11) Bäuerlein, F. J. B.; Saha, I.; Mishra, A.; Kalemanov, M.; Martínez-Sánchez, A.; Klein, R.; Dudanova, I.; Hipp, M. S.; Hartl, F. U.; Baumeister, W.; et al. *In situ* architecture and cellular interactions of polyQ inclusions. *Cell* **2017**, *171*, 179−187.

(12) Olzscha, H.; Schermann, S. M.; Woerner, A. C.; Pinkert, S.; Hecht, M. H.; Tartaglia, G. G.; Vendruscolo, M.; Hayer-Hartl, M.; Hartl, F. U.; Vabulas, R. M. Amyloid-like aggregates sequester numerous metastable proteins with essential cellular functions. *Cell* **2011**, *144*, 67−78.

(13) Donaldson, K. M.; Li, W.; Ching, K. A.; Batalov, S.; Tsai, C.-C.; Joazeiro, C. A. P. Ubiquitin-mediated sequestration of normal cellular proteins into polyglutamine aggregates. *Proc. Natl. Acad. Sci. U. S. A.* **2003**, *100* (15), 8892−8897.

(14) Buchanan, L. E.; Carr, J. K.; Fluitt, A. M.; Hoganson, A. J.; Moran, S. D.; de Pablo, J. J.; Skinner, J. L.; Zanni, M. T. Structural motif of polyglutamine amyloid fibrils discerned with mixed-isotope infrared spectroscopy. *Proc. Natl. Acad. Sci. U. S. A.* **2014**, *111* (16), 5796−5801.

(15) Xiong, K.; Punihaole, D.; Asher, S. A. UV resonance Raman spectroscopy monitors polyglutamine backbone and side chain hydrogen bonding and fibrillization. *Biochemistry* **2012**, *51*, 5822−5830.

(16) Devitt, G.; Howard, K.; Mudher, A.; Mahajan, S. Raman Spectroscopy: An emerging tool in neurodegenerative disease research and diagnosis. *ACS Chem. Neurosci.* **2018**, *9* (3), 404−420.

(17) Matlahov, I.; van der Wel, P. C. Conformational Studies of Pathogenic Expanded Polyglutamine Protein Deposits from Huntington's Disease. *Exp. Biol. Med.* **2019**, *244*, 1584.

(18) Warner, J. B.; Ruff, K. M.; Tan, P. S.; Lemke, E. A.; Pappu, R. V.; Lashuel, H. A. Monomeric Huntingtin exon 1 has similar overall structural features for wild-type and pathological polyglutamine lengths. *J. Am. Chem. Soc.* **2017**, *139* (41), 14456−14469.

(19) Crick, S. L.; Jayaraman, M.; Frieden, C.; Wetzel, R.; Pappu, R. V. Fluorescence correlation spectroscopy shows that monomeric polyglutamine molecules form collapsed structures in aqueous solutions. *Proc. Natl. Acad. Sci. U. S. A.* **2006**, *103* (45), 16764−16769.

(20) Iwata, A.; Christianson, J. C.; Bucci, M.; Ellerby, L. M.; Nukina, N.; Forno, L. S.; Kopito, R. R. Increased susceptibility of cytoplasmic over nuclear polyglutamine aggregates to autophagic degradation. *Proc. Natl. Acad. Sci. U. S. A.* **2005**, *102* (37), 13135−13140.

(21) Liu, Y.; Wolstenholme, C. H.; Carter, G. C.; Liu, H.; Hu, H.; Grainger, L. S.; Miao, K.; Fares, M.; Hoelzel, C. A.; Yennawar, H. P.; et al. Modulation of fluorescent protein chromophores to detect protein aggregation with turn-on fluorescence. *J. Am. Chem. Soc.* **2018**, *140*, 7381−7384.

(22) Mangiarini, L.; Sathasivam, K.; Seller, M.; Cozens, B.; Harper, A.; Hetherington, C.; Lawton, M.; Trottier, Y.; Lehrach, H.; Davies, S. W.; et al. Exon 1 of the HD gene with an expanded CAG repeat is sufficient to cause a progressive neurological phenotype in transgenic mice. *Cell* **1996**, *87*, 493−506.

(23) Tsien, R. Y. The Green Fluorescent Protein. *Annu. Rev. Biochem.* **1998**, *67* (1), 509−544.

(24) Bhattacharya, M.; Mukhopadhyay, S. Studying Protein Misfolding and Aggregation by Fluorescence Spectroscopy. In *Reviews in Fluorescence 2015*; Geddes, C., Ed.; Springer: Cham, 2016; Vol. *8*.
(25) Kozlowski, L. P. Proteome-pI: proteome isoelectric point database. *Nucleic Acids Res.* **2017**, *45*, D1112−D1116.
(26) Freudiger, C. W.; Min, W.; Saar, B. G.; Lu, S.; Holtom, G. R.; He, C.; Tsai, J. C.; Kang, J. X.; Xie, X. S. Label-free biomedical imaging with high sensitivity by stimulated Raman scattering microscopy. *Science* **2008**, *322* (5909), 1857−1861.
(27) Shen, Y.; Xu, F.; Wei, L.; Hu, F.; Min, W. Live-cell quantitative imaging of proteome degradation by stimulated Raman scattering. *Angew. Chem., Int. Ed.* **2014**, *53*, 5596−5599.
(28) Wei, L.; Shen, Y.; Xu, F.; Hu, F.; Harrington, J. K.; Targoff, K. L.; Min, W. Imaging complex protein metabolism in live organisms by stimulated Raman scattering microscopy with isotope labeling. *ACS Chem. Biol.* **2015**, *10* (3), 901−908.
(29) Zhang, J.; Yan, S.; He, Z.; Ding, C.; Zhai, T.; Chen, Y.; Li, H.; Yang, G.; Zhou, X.; Wang, P. Small unnatural amino acid carried Raman tag for molecular imaging of genetically targeted proteins. *J. Phys. Chem. Lett.* **2018**, *9* (16), 4679−4685.
(30) Min, W.; Freudiger, C. W.; Lu, S.; Xie, X. S. Coherent Nonlinear Optical Imaging: Beyond Fluorescence Microscopy. *Annu. Rev. Phys. Chem.* **2011**, *62* (1), 507−530.
(31) Perney, N. M.; Braddick, L.; Jurna, M.; Garbacik, E. T.; Offerhaus, H. L.; Serpell, L. C.; Blanch, E.; Holden-Dye, L.; Brocklesby, W. S.; Melvin, T. Polyglutamine aggregate structure *in vitro* and *in vivo*; new avenues for coherent anti-stokes Raman scattering microscopy. *PLoS One* **2012**, *7* (7), No. e40536.
(32) Wei, L.; Hu, F.; Shen, Y.; Chen, Z.; Yu, Y.; Lin, C.-C.; Wang, M. C.; Min, W. Live-cell imaging of alkyne-tagged small biomolecules by stimulated Raman scattering. *Nat. Methods* **2014**, *11* (4), 410−412.
(33) Piez, K. A.; Eagle, H. The free amino acid pool of cultured human cells. *J. Bol. Chem.* **1958**, *231*, 533−545.
(34) Li, L.; Liu, H.; Dong, P.; Li, D.; Legant, W. R.; Grimm, J. B.; Lavis, L. D.; Betzig, E.; Tjian, R.; Liu, Z. Real-time imaging of Huntingtin aggregates diverting target search and gene transcription. *eLife* **2016**, *5*, 17056.
(35) Ji, M.; Arbel, M.; Zhang, L.; Freudiger, C. W.; Hou, S. S.; Lin, D.; Yang, X.; Bacskai, B. J.; Xie, X. S. Label-free imaging of amyloid plaques in Alzheimer's disease with stimulated Raman scattering microscopy. *Sci. Adv.* **2018**, *4*, No. eaat7715.
(36) Hackett, M. J.; McQuillan, J. A.; El-Assaad, F.; Aitken, J. B.; Levina, A.; Cohen, D. D.; Siegele, R.; Carter, E. A.; Grau, G. E.; Hunt, N. H.; et al. Chemical alterations to murine brain tissue induced by formalin fixation: implications for biospectroscopic imaging and mapping studies of disease pathogenesis. *Analyst* **2011**, *136*, 2941−2952.
(37) Sittler, A.; Lurz, R.; Lueder, G.; Priller, J.; Hayer-Hartl, M. K.; Hartl, F. U.; Lehrach, H.; Wanker, E. E. Geldanamycin activates a heat shock response and inhibits Huntingtin aggregation in a cell culture model of Huntington's disease. *Hum. Mol. Genet.* **2001**, *10* (12), 1307−1315.
(38) Peskett, T. R.; Rau, F.; O'Driscoll, J.; Patani, R.; Lowe, A. R.; Saibil, H. R. A liquid to solid phase transition underlying pathological Huntingtin exon1 aggregation. *Mol. Cell* **2018**, *70*, 588−601.
(39) Lee, H. J.; Zhang, D.; Jiang, Y.; Wu, X.; Shih, P.-Y.; Liao, C.-S.; Bungart, B.; Xu, X.-M.; Drenan, R.; Bartlett, E.; et al. Label-free vibrational spectroscopic imaging of neuronal membrane potential. *J. Phys. Chem. Lett.* **2017**, *8*, 1932−1936.
(40) Muchowski, P. J.; Schaffar, G.; Sittler, A.; Wanker, E. E.; Hayer-Hartl, M. K.; Hartl, F. U. Hsp70 and Hsp40 chaperones can inhibit self-assembly of polyglutamine proteins into amyloid-like fibrils. *Proc. Natl. Acad. Sci. U. S. A.* **2000**, *97* (14), 7841−7846.
(41) Hartl, F. U.; Bracher, A.; Hayer-Hartl, M. Molecular chaperones in protein folding and proteostasis. *Nature* **2011**, *475*, 324−332.
(42) Orr, H. T.; Zoghbi, H. Y. Trinucleotide repeat disorders. *Annu. Rev. Neurosci.* **2007**, *30*, 575−621.
(43) Guo, Q.; Lehmer, C.; Martínez-Sánchez, A.; Rudack, T.; Beck, F.; Hartmann, H.; Pérez-Berlanga, M.; Frottin, F.; Hipp, M. S.; Hartl, F. U.; et al. *In situ* structure of neuronal C9orf72 poly-GA aggregates reveals proteasome recruitment. *Cell* **2018**, *172*, 696−705.
(44) Ash, P. E. A.; Bieniek, K. F.; Gendron, T. F.; Caulfield, T.; Lin, W.-L.; DeJesus-Hernandez, M.; van Blitterswijk, M. M.; Jansen-West, K.; Paul, J. W.; Rademakers, R.; et al. Unconventional translation of C9orf72 GGGGCC expansion generates insoluble polypeptides specific to c9FTD/ALS. *Neuron* **2013**, *77*, 639−646.
(45) Ennis, S. R.; Kawai, N.; Ren, X.; Abdelkarim, G. E.; Keep, R. F. Glutamine Uptake at the Blood-Brain Barrier Is Mediated by N-System Transport. *J. Neurochem.* **1998**, *71* (6), 2565−2573.

https://dx.doi.org/10.1021/acscentsci.9b01196
ACS Cent. Sci. 2020, 6, 478−486